

Three Dimensional Modeling of Short Fiber Reinforced Composites with the Extended Finite Element Method

Matthew G. Pike*, and Caglar Oskay†

Department of Civil and Environmental Engineering
Vanderbilt University
Nashville, TN 37235

Abstract

This manuscript presents a modeling approach based on the extended finite element method (XFEM) for modeling three dimensional short fiber composites. Short fibers are incorporated into the XFEM framework as deformable elastic two dimensional rectangular planar inclusions. Enrichment equations account for both the presence of axial deformable fibers within the composite domain and the progressive debonding on the fiber matrix interfaces. The proposed manuscript provides a modeling strategy particularly suitable for high aspect ratio inclusions with fiber matrix debonding capabilities in three dimensions. The performance of the proposed XFEM model is assessed by comparing model predictions to the direct finite element method.

Keywords: 3D Extended Finite Element Method, short fiber composites, interface debonding, random short fibers

1 Introduction

Incorporation of short fibers enhance the mechanical properties of many engineered materials, including increase in elastic modulus, load carrying capacity, flexural strength and flexural toughness [1, 2, 3]. The short fiber composite materials also provide unique and favorable functional properties, including crack control, electromagnetic field shielding and self sensing (e.g. [4, 5, 6]). This manuscript presents an extended finite element method (XFEM) to model high aspect ratio short fiber composites in three dimensions. In the proposed approach,

*Author address: VU Station B#351831, 2301 Vanderbilt Place, Nashville, TN 37235. Email: matthew.g.pike@vanderbilt.edu

†Corresponding author address: VU Station B#351831, 2301 Vanderbilt Place, Nashville, TN 37235. Email: caglar.oskay@vanderbilt.edu

fibers are represented as two dimensional elastic deformable planar rectangles with progressive debonding capabilities on the fiber-matrix interface.

The elastic and strength properties of short fiber reinforced composites have been modeled using the micromechanical approach based on Eshelby's solution of ellipsoidal inclusions combined with the Mori-Tanaka scheme [7, 8], and Hashin-Strichman bounds [9], and others. While micromechanical based analysis provides good estimates of the homogenized properties of the composite, localized failure mechanisms as well as debonding between the constituents are not directly modeled. A fuller understanding of the idealized failure response can be gained based on detailed numerical analysis of the resolved representative volume elements (RVEs) [10, 11]. This approach is useful for understanding fiber interactions within dilute concentrations [12, 13], but direct numerical analysis in the presence of a large number of high aspect ratio fibers is computationally infeasible. This is because, the discretization of the domain must utilize small elements to resolve the fiber and ensure mesh compatibility between the fibers and the matrix for an accurate response.

Various methods have been proposed to eliminate the need to finely discretize the entire domain with finite elements, including the variational multiscale enrichment method, in which there is fine scale representation at small subdomains around material heterogeneity (see e.g., [14, 15, 16]). Approaches to eliminate the need for direct resolution of individual fibers in reinforced composites have been previously proposed. Analytical models for short fiber composites have been developed to capture the elastic response and estimate fiber stresses [17, 18]. Numerical models have been also developed to account for embedded fibers by idealizing the fibers as truss elements using their end coordinates, without explicitly discretizing within the finite element mesh [19, 20].

Applying the principles of XFEM is an alternative approach to model the behavior of fiber-reinforced composites. With the XFEM approach, the need to discretize individual fibers and the need to enforce mesh compatibility between the fibers and matrix phase is eliminated. The approximation basis enrichment strategy of XFEM furnishes the standard finite element basis with additional nodal enrichment functions capable of representing inhomogeneities and discontinuities within the problem domain without explicitly representing them through meshing [21, 22]. The enrichment functions are known a-priori to represent the response well within the whole domain or a subdomain of the problem, around strong or weak discontinuities and incorporated such that the partition of unity property for the enrichment is satisfied [23]. XFEM has been successfully used to model strong and weak discontinuities [24, 25, 26], multiple cracks and inclusions [27, 28, 29], as well as cohesive behavior [30, 31] in a 2-D setting.

XFEM modeling of cracks in three dimensional problems has been recently proposed for fatigue and dynamic propagation [32, 33, 34, 35], amongst others. Duarte et al. [36] accounted for the presence of internal boundaries and geometries in a 3-D domain. Three dimensional

woven fiber composites were modeled using XFEM by Moës et al. [37]. The modeling of cylindrical fibers has been proposed by Soghrati and Geubelle [38]. Oswald et al. [39] developed an approach to model carbon nanotube and thin films using 3-D XFEM.

Similar in principals to XFEM modeling, methods to model inclusion discontinuities have been proposed (e.g., [40, 41, 42, 43]). Radtke et al. [44, 45] were the first to model high aspect ratio fibers as zero measure elastic inclusions in the context of short fiber reinforced composites. The strong discontinuity present due to tangential debonding at the fiber-matrix interface was modeled with a Heaviside enrichment function. Tangential slip was idealized based on a non-linear cohesive law, while the normal fiber-matrix interface separation was not considered. Previous work performed by the authors developed a two dimensional formulation of high aspect ratio fiber composites using XFEM. An XFEM model for random rigid short fibers in an elastic domain was proposed in [46]. Refs. [47, 48] formulated a progressive failure model for random short fiber reinforced composite materials for elastic deformable fiber inclusions that accounts for the presence of multiple fibers within close proximity.

This manuscript builds on the ideas of Radtke and co workers as wells as Refs. [46]-[48], and presents a three dimensional XFEM model for short fiber composites. In a three dimensional setting, high aspect ratio fibers are modeled as two dimensional planar rectangular inclusions. The fibers are taken to be elastic and deformable in the axial direction, which is the dominant deformation mechanism for short fibers embedded in a matrix domain. Fiber and debonding enrichment functions account for the presence of the fibers within the composite domain, and idealize the progressive debonding on the fiber-matrix interfaces, respectively. The capabilities of the proposed XFEM model are verified against the direct finite element method and the performance of the model is assessed. The proposed formulation includes the following key features: (1) The high aspect ratio fiber is modeled as a two dimensional rectangular inclusion in three dimensions, where the resolved faces are used to initiate debonding; (2) 3-D enrichment functions are used to account for traction-separation behavior and the strain discontinuity at fiber-matrix interfaces; (3) Multiple zero measure inclusions are incorporated in the same element to allow the presence of fibers close to one another without excessive localized meshing; and (4) The present formulation accounts for decohesion in both tangential and normal directions.

The remainder of this manuscript is organized as follows. In Section 2, the XFEM method for a three dimensional domain is presented. Section 3 provides the governing equations and computational formulation, particularly the details of the numerical integration for various enrichment types. Numerical verification studies to assess the performance of this approach are presented in Section 4. Conclusions and future research directions are discussed in Section 5.

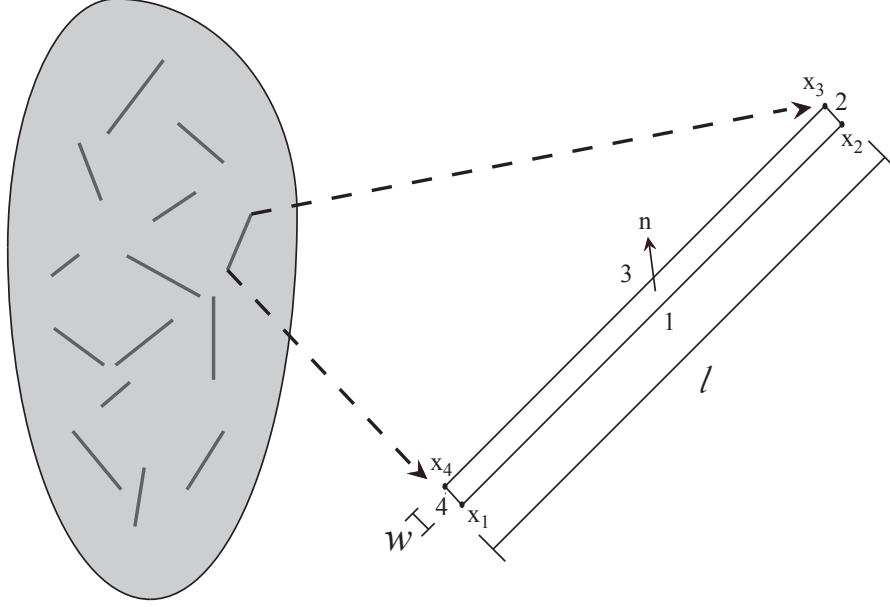


Figure 1: A schematic representation of a short fiber composite domain with two-dimensional fiber identification.

2 3-D Enrichment Functions

In this manuscript, short fibers in a three dimensional XFEM domain are modeled as two dimensional objects. Fibers are taken to have high aspect ratios with $l \gg w \gg t$, where l , w , and t denote length, width and thickness of the fiber respectively (Fig. 1). Fibers of such geometry are employed in [2, 49, 50] in a cement domain. Other work utilizing rectangular short fibers of different sizes and materials has also been performed in Refs. [51, 52, 53]. Considering no twisting, a fiber is defined by three corner points of the thin rectangle, which forms the plane of the fiber along with its width. Fibers are modeled as two dimensional inclusions due their high aspect ratio.

The displacement field discretization that accounts for the planar fibers is expressed as [48]:

$$\mathbf{u}(\mathbf{x}) = \sum_{a=1}^{n_n} N_a(\mathbf{x}) \hat{\mathbf{u}}_a + \sum_{\alpha=1}^n \left[\sum_{b=1}^{n_{\text{en}}^{\alpha}} N_{\mathcal{I}_b^{\alpha}}(\mathbf{x}) \psi_{\alpha}(\mathbf{x}) \hat{\mathbf{c}}_{b\alpha} \right] + \sum_{\alpha=1}^n \left[\sum_{c=1}^{n_{\text{en}}^{\alpha}} N_{\mathcal{I}_c^{\alpha}}(\mathbf{x}) \Upsilon_{\alpha}(\mathbf{x}) \hat{\mathbf{d}}_{c\alpha} \right] \quad (1)$$

where, the displacement field is denoted as \mathbf{u} ; the space coordinate is \mathbf{x} ; n_n the total number of mesh nodes in the finite element discretization; n is the number of fibers, n_{en}^{α} is the number of enriched nodes for fiber α ; N_a , the standard finite element shape function associated with node a ; $\hat{\mathbf{u}}_a$, $\hat{\mathbf{c}}_{b\alpha}$ and $\hat{\mathbf{d}}_{c\alpha}$ the nodal coefficients of the standard, fiber enrichment and debonding enrichments for each fiber α , respectively; \mathcal{I}^{α} is the index set of enriched nodes for fiber α ; $\mathcal{I}_a^{\alpha} \in \mathcal{I}^{\alpha}$ the index of an enriched node, a . The fiber enrichment and the debonding enrichment

functions are denoted as ψ_α and Υ_α , respectively.

The first right hand side term in Eq. 1 represents the standard finite element approximation. The second term represents the presence of the fiber within the domain, in which the strain discontinuity in the approximation space is a function of the fiber enrichment function, ψ_α . The third term corresponds to the separation along the face of the fiber and the matrix due to the progressive loss of cohesion between them.

2.1 Fiber enrichment function

The enrichment function for the fiber is expressed in terms of a distance function to the fiber body. For simplicity, α , which indicates the the fiber, is omitted in this and the next section.

The reinforcing fiber is taken to be entirely embedded in the open bounded domain of the three dimensional composite body, $\Omega \subset \mathbb{R}^3$. The distance function associated with the fiber body, $\phi_c(\mathbf{x})$, is expressed as:

$$\phi_c(\mathbf{x}) = \|\mathbf{x} - \mathbf{x}_p\| \quad (2)$$

where, \mathbf{x}_p is any point on the fiber domain, and ϕ_c represents the distance from any point in the domain to the fiber body.

The distance function from Eqs. 2 is used to express the enrichment function for the fiber as the smallest distance between any point and the fiber domain:

$$\psi(\mathbf{x}) = \min(\phi_c(\mathbf{x})) \quad (3)$$

The enrichment function is displayed in Fig. 2a for a randomly placed short fiber in a three dimensional domain, where the value of the enrichment function increases from blue (zero) to red (highest). Cross sectional contours of the enrichment function are shown in Figs. 2b-c. The enrichment function, ψ , incorporates a strain discontinuity mode along the fiber position and the displacements around the fiber can be captured without explicitly discretizing the fiber domain. The form of Eq. 3 for the enrichment function ensures that the approximation basis captures the strain discontinuity but stays smooth otherwise around the sides and face of the fiber.

2.2 Debonding enrichment function

The debonding enrichment function describes the debonding between the fiber and the matrix and introduces a strong discontinuity in the displacement field. To model the shape of the debonding between the fiber and matrix interface in three dimensions, a Heaviside function is used to represent the physical separation in the normal and tangential directions. Since

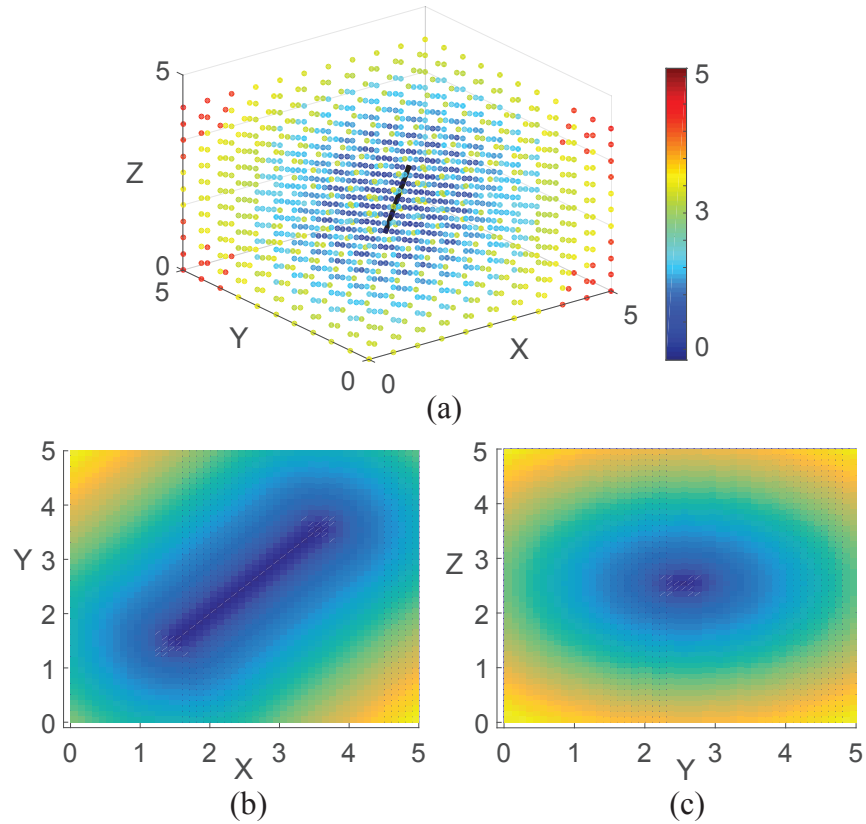


Figure 2: Short fiber inclusion enrichment function for three dimensions. Blue represents values close to 0 and red represented the highest value: (a) three dimensional view with the black line representing the fiber; (b) fiber enrichment values in the X-Y plane; (c) fiber enrichment values in the Y-Z plane.

the fiber is idealized as planar, the debonding is considered along the plane of the fiber. The possibility of debonding along the sides of the fiber is not considered in this work.

The debonding enrichment function is expressed in terms of the level set functions describing the fiber domain. The level set associated with the plane of the fiber $\phi_f(\mathbf{x})$, is expressed as:

$$\phi_f(\mathbf{x}) = \hat{\mathbf{n}} \cdot (\mathbf{x} - \mathbf{x}_c) \quad (4)$$

where $\hat{\mathbf{n}}$ is the normal vector to the fiber and \mathbf{x}_c is a reference point on the plane of the fiber, set to the center of the fiber. ϕ_f divides the domain along the plane of the fiber and is the signed distance function, which vanishes on the fiber plane. The level set functions for the fiber edges, e , are expressed as:

$$\phi_e(\mathbf{x}) = (\mathbf{x} - \mathbf{x}_{x_e}) \cdot \mathbf{t}_e; \quad e = 1, 2, 3, 4 \quad (5)$$

in which, e represents the fiber edge, \mathbf{t}_e denotes the tangent at the fiber edge, \mathbf{x}_{x_1} is a end point on the fiber edge, e (i.e. fiber corner point). ϕ_e provides the zero level set along the plane normal to the fiber edge, e , with positive values on one side of the domain cut by ϕ_e and negative elsewhere in the domain.

The debonding enrichment function for the fiber is then expressed in terms of the discontinuity functions as:

$$\Upsilon(\mathbf{x}) = H(\phi_f) \left(\prod_{e=1}^4 H(-\phi_e) \right) \quad (6)$$

The debonding enrichment function, Υ , is employed to capture debonding along both normal and tangential directions. Interfacial damage in directions normal and tangential to the fibers has been observed experimentally in fiber reinforced composites (see, e.g. [54]).

3 Governing Equations and Computational Formulation

The mechanical equilibrium and boundary conditions within the three dimensional domain for a composite is expressed as:

$$\nabla \cdot \boldsymbol{\sigma}(\mathbf{x}, t) = 0; \quad \mathbf{x} \in \Omega \quad (7)$$

$$\boldsymbol{\sigma} = \mathbf{L}(\mathbf{x}) : \boldsymbol{\epsilon}(\mathbf{x}, t) \quad (8)$$

$$\mathbf{u}(\mathbf{x}, t) = \tilde{\mathbf{u}}(\mathbf{x}, t); \quad \mathbf{x} \in \Gamma_u \quad (9)$$

$$\boldsymbol{\sigma} \cdot \mathbf{n} = \tilde{\mathbf{t}}(\mathbf{x}, t); \quad \mathbf{x} \in \Gamma_t \quad (10)$$

in which, $\boldsymbol{\sigma}$ is the stress tensor; ∇ the divergence operator; and $\boldsymbol{\epsilon}$ denotes the strain tensor. The strain is taken to be the symmetric gradient of the displacement field ($\boldsymbol{\epsilon} = \nabla^s \mathbf{u}$). \mathbf{L} is the tensor of elastic moduli of the matrix or of the fiber, as a function of position within the domain, taken to be symmetric and positive definite. $\tilde{\mathbf{u}}$ and $\tilde{\mathbf{t}}$ are the prescribed boundary displacements and tractions defined on boundaries Γ_u and Γ_t , respectively, such that $\Gamma_u \cap \Gamma_t = \emptyset$ and $\partial\Omega = \Gamma_u \cup \Gamma_t$. The domains of fiber α , and the matrix are denoted as Ω_α and Ω_m , respectively. The short fibers do not intersect with each other (i.e., $\Omega = \Omega_m \cup \bigcup_{\alpha=1}^n \Omega_\alpha$) and are taken to be embedded fully in the matrix. In this study, the matrix and fibers are taken to be elastic. It is straightforward to consider non linear or damage behavior within the matrix as demonstrated in a 2-D setting in Ref. [47].

Across the fiber-matrix interface the traction continuity is expressed as:

$$[[\mathbf{T}]] = [[\boldsymbol{\sigma} \cdot \mathbf{n}]] = 0 \quad \mathbf{x} \in \Gamma_\alpha \equiv \partial\Omega_m \cap \partial\Omega_\alpha \quad \alpha = 1, 2, \dots, n \quad (11)$$

in which the traction \mathbf{T} , is defined in the local coordinate system as a function of the normal and tangential components; \mathbf{n} is the outward unit vector to the boundary; and $[[\cdot]]$ is the jump operator. Γ_α represents the interface between the fiber, α , and the matrix.

A cohesive law describing the relationship between surface traction and separation represents the physical deterioration that occurs at the fiber-matrix interface. A bilinear cohesive law is considered:

$$T_i([\hat{\mathbf{u}}_i]) = \begin{cases} \frac{[[\hat{\mathbf{u}}_i]]}{d_i} t_i^{\max} & d_i \geq [[\hat{\mathbf{u}}_i]] \geq 0 \\ \frac{t_i^{\max}}{d_i^{\text{crit}} - d_i} (d_n^{\text{crit}} - [[\hat{\mathbf{u}}_i]]) & d_i^{\text{crit}} \geq [[\hat{\mathbf{u}}_i]] \geq d_i \\ 0 & [[\hat{\mathbf{u}}_i]] \geq d_i^{\text{crit}} \end{cases} \quad (12)$$

in which, $[[\hat{\mathbf{u}}_i]]$, is the displacement jump vector (i.e. separation) defined in the local coordinate system; d_i the cohesive characteristic separation length for the normal and tangential directions ($d_i = d_n, d_{t_1}, d_{t_2}$); t_i^{\max} denotes the ultimate traction; and d_i^{crit} is the maximum displacement jump.

To develop the weak form of the model from Eqs. 7-11, standard finite element procedure is used and the weak form is expressed as follows:

$$\int_{\Omega_m} \boldsymbol{\sigma} : \delta\boldsymbol{\epsilon} d\Omega + \sum_{\alpha=1}^n \int_{\Gamma_\alpha} \mathbf{T} \cdot \delta[[\mathbf{u}]] d\Gamma + \sum_{\alpha=1}^n \int_{\Omega_\alpha} \boldsymbol{\sigma} : \delta\boldsymbol{\epsilon} d\Omega - \int_{\Gamma_t} \tilde{\mathbf{t}} \cdot \delta\mathbf{u} d\Gamma = 0 \quad (13)$$

where, $\delta\mathbf{u}$ denotes the test function; and $\delta\boldsymbol{\epsilon}$ the gradient of the test function.

With the condition that the short fibers have high aspect ratios, we assume that tractions

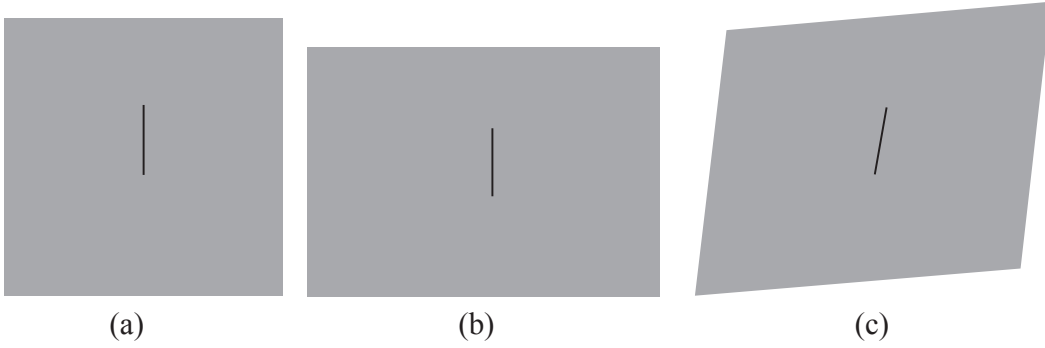


Figure 3: 3-D direct finite element simulation (cross section cut at the center of the fiber width): (a) initial RVE with the short vertical fiber before tensile loading; (b) amplified deformed RVE with the short vertical fiber after tensile loading; and (c) amplified deformed RVE with the short vertical fiber after shear loading.

along the two opposing faces of a fiber in the thickness direction are uniform. Debonding along the two faces of a fiber would typically occur concurrently for a short fiber embedded in a matrix under the traction conditions. However, the fiber-matrix debonding is likely to initiate at a weak spot at one face of the fiber. Upon complete debonding at the weak face, the tractions along the opposing (unbonded) face relax. Since the width of the fiber is significantly smaller than the length, $l_\alpha/w_\alpha \gg 1$, tractions across the width of the fiber are also taken to be uniform.

Fibers are assumed to be fully embedded in the domain, have high aspect ratios and subjected to approximately uniform tractions along the length of the fiber. No significant shear stress or bending moment develops within the domain of the fiber and the stress in the fiber is taken to be predominately axial. These considerations are verified using direct finite element simulations where the fiber is resolved with highly resolved meshes in three dimensions. Fig. 3 displays a finite element simulation of a cross section cut of a vertical short fiber ($l/w/t = 1000/20/1$) in a matrix domain subject to tensile and shear loading. Fig. 3a displays the initial state, where Fig. 3b shows the deformation state under tensile loading. The displacements are amplified for visualization purposes and the figures shows that fiber bending is insignificant. Fig. 3c demonstrates the deformation profile under shear loading, which also exhibit insignificant bending in the fiber.

With the high aspect ratio fiber and the assumption of uniform stress across the width of the fiber, the third term in Eq. 13 approximated as:

$$\int_{\Omega_\alpha} \boldsymbol{\sigma} : \delta \boldsymbol{\epsilon} d\Omega \simeq A_{f\alpha} \int_{\Omega_\alpha} \sigma_f^\alpha \delta \epsilon_f^\alpha d\Omega \quad (14)$$

where, $A_{f\alpha}$ is the cross sectional area of the fiber. The axial stress in fiber α , is taken to be

proportional to the axial strain (i.e., $\sigma_f^\alpha = E_f \epsilon_f^\alpha$), where E_f is the elastic modulus of the fiber.

The domain of the matrix is taken to occupy the entire domain, since the domains of the fibers are vanishingly small and modeled as zero measure inclusions (i.e., 2-D). The weak form of the governing equations for the fiber composites then becomes:

$$\int_{\Omega} \boldsymbol{\sigma} : \delta \boldsymbol{\epsilon} d\Omega + \sum_{\alpha=1}^n \int_{\Gamma_\alpha} \mathbf{T} \cdot \delta[\mathbf{u}] d\Gamma + \sum_{\alpha=1}^n A_{f\alpha} E_f \int_{\Omega_\alpha} \epsilon_f^\alpha \delta \epsilon_f^\alpha d\Omega - \int_{\Gamma_t} \tilde{\mathbf{t}} \cdot \delta \mathbf{u} d\Gamma = 0 \quad (15)$$

XFEM is employed to discretize and evaluate the governing equations (Eqs. 7-15). The standard Ritz-Galerkin procedure is utilized and results in a nonlinear system, which is incrementally evaluated using the Newton-Raphson method. The 3-D formulation associated with the extended finite element discretization generally follows the 2-D counterpart, which is described in detail in Refs. [47, 48]. In what follows, we describe the numerical integration of various enriched elements, necessary to evaluate Eq. 15 in the XFEM context.

3.1 Numerical integration

In XFEM, the extent of the subdomain around an inclusion that is enriched is chosen based on the geometry or the discretization. A geometry-based approach is considered for modeling cracks using specified a radius around the crack tip since the stress fields around the crack tip vary as a function of the distance from the tip. In this work, the enrichment domain is chosen based on the discretization since the enrichments functions accurately represent the local behavior around the inclusion. Various methods to integrate enrichment functions in three dimensions have been investigated in Refs. [55, 56, 57].

In this manuscript, the 3-D domain is comprised of a standard mesh of hexagonal elements with four different element types: (1) far field elements; (2) partial enriched elements; (3) fully enriched elements; and (4) fully enriched elements that also have partial enrichment.

The *far field elements* have no enrichment and use standard quadrature rules with eight integration points in a tri-linear hexagonal element. *Partially enriched elements* include some nodal enrichment from one or multiple fiber inclusions but are not fully enriched (i.e. one or more fibers lie in elements adjacent to the current element). Since no displacement discontinuity exists, standard quadrature rule is employed with eight integration points in a hexagonal element. *Fully enriched elements* are those crossed by one or multiple fibers. Considering the position of each fiber, the hexagonal element domain is split into tetrahedral sub domains (see Fig. 4) using Delaunay triangulation. The tetrahedral sub domains are placed such that no sub domain cross the domain of the fiber and line up with the fiber interface, to ensure that the components of the enrichment function for the fiber edges and domain level sets are integrated separately. Each tetrahedral sub element contains 11 integration points creating

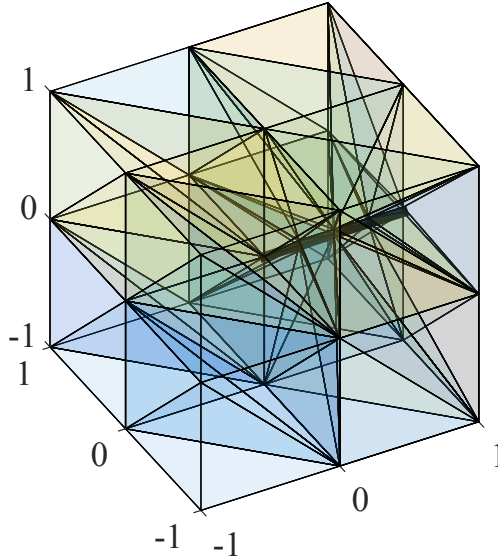


Figure 4: 3-D visualization of tetrahedral sub elements in an hexagonal enrichment element. Thick black line represents the fiber inclusion.

high order integration in the enriched element. *Fully enriched elements that also have partial enrichment:* use the same element splitting rules as in the fully enriched elements, and use higher order integration rules for each sub element.

The cohesive interface integration is performed using two dimensional Gauss quadrature on the two dimensional domain of the fiber. The interface integration is independent of the domain discretization. The fiber-matrix interface Γ_α is divided into multiple rectangular domains, based on the length of the fiber, l_α . Each rectangular domain uses a 4-point quadrature rule to perform the cohesive integration on the fiber domain.

4 Numerical Examples

In this section, the performance of the proposed model in capturing the response of short fiber reinforced composites is assessed. The first example investigates the accuracy characteristics of a randomly oriented single fiber embedded in a domain with elastic matrix perfectly bonded with the fiber, as well as in the presence progressive debonding along the fiber-matrix interface. The second example investigates the fiber-matrix debonding and localized stresses for a case with two randomly oriented fibers in close neighborhood with each other. The effects of the orientation of the fiber interface within the domain in relation to the applied loading, the influence of the aspect ratio of the fiber with respect to the interface debonding are presented next. The last study evaluates the response of a domain reinforced by multiple fibers.

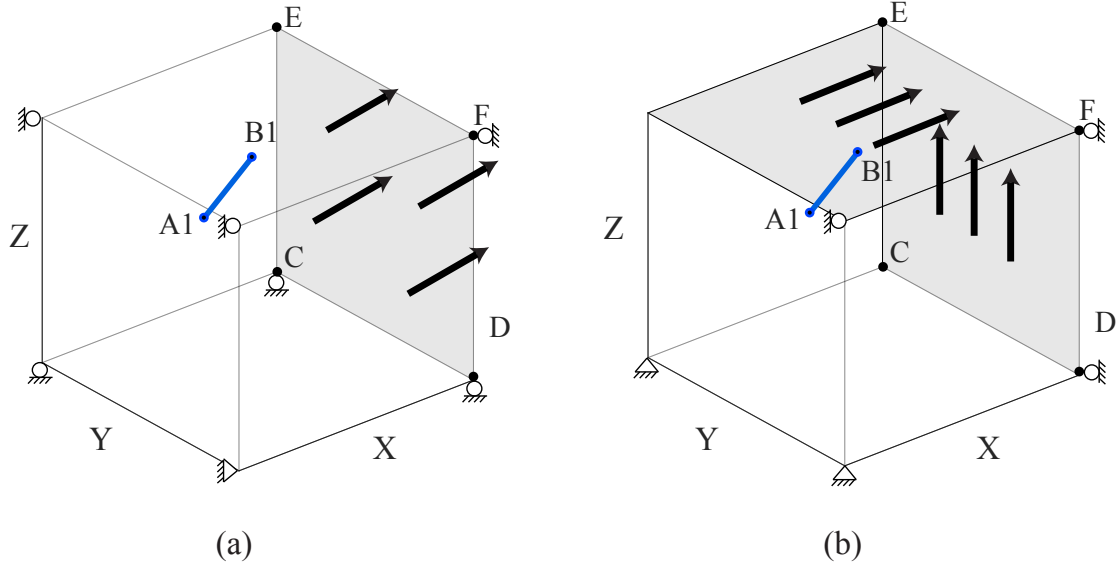


Figure 5: Geometry and boundary conditions of the single fiber inclusion examples: (a) Tensile loading case with loading at the right Y-Z face (shaded area); and (b) shear loading case with loading at the right Y-Z face and top X-Y face (shaded area).

4.1 Single fiber inclusion

The schematic representations of the model problems are shown in Fig. 5. Two cases are investigated: a cubic domain subjected to uniform displacement controlled tensile loading (Fig. 5a); and a domain subject to uniform displacement controlled shear loading (Fig. 5b). Symmetric boundary conditions are imposed on the left, bottom and back faces for the tensile case. The shear loading case utilizes fixed boundary conditions in all three directions at the left bottom edge and fixed z direction boundary conditions on back face. The edge length of the domain is 4 mm. The length of the fiber is 1mm. The matrix material is taken to be concrete with the Young's modulus and Poisson's ratio set as 14 GPa and 0.3, respectively. The fiber is taken to be a high strength fiber with the Young's modulus of 207 GPa, and width and thickness of $20 \mu\text{m}$ and $1 \mu\text{m}$, respectively. In this example, the fiber orientation parallel to the x direction with the fiber body positioned with Euler angles of 63° , 106° and 32° .

When included, progressive debonding at the fiber-matrix interfaces is modeled using the bilinear cohesive zone law (defined in Eq. 12) for both the proposed model and the reference simulations. The peak normal traction and normal cohesive characteristic separation length are set as 10 MPa and 1 nm respectively. The peak shear traction and shear cohesive characteristic separation lengths are set identical to their normal counterparts. The maximum cohesive separation length is taken as 8 nm both for normal and shear directions [58].

In the proposed XFEM model, the domain is discretized with a uniform grid (hexahedra) of various mesh densities ranging from 64 elements up to approximately 33,000 elements

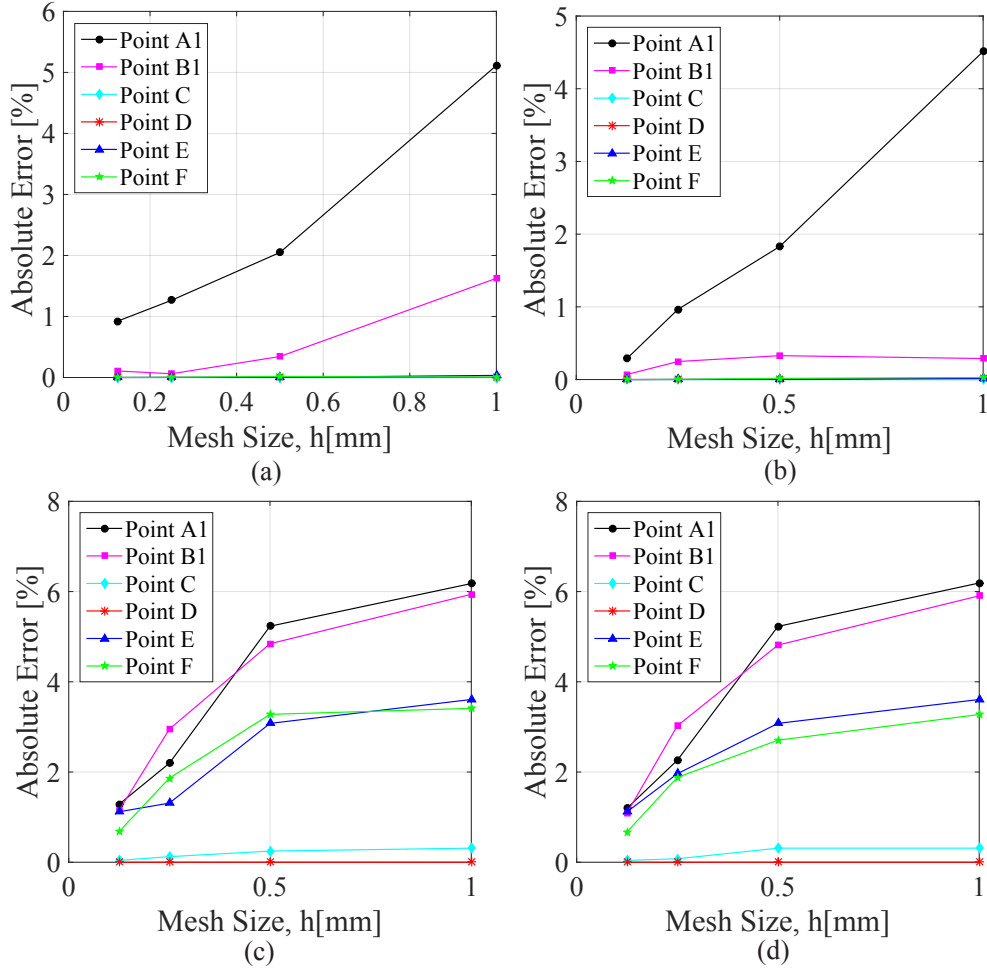


Figure 6: Pointwise error as a function of mesh density: (a) elastic domain with tensile loading; (b) domain with progressive interface debonding with tensile loading; (c) elastic domain with shear loading; and (d) domain with progressive interface debonding with shear loading.

with corresponding element sizes of $h=1$ mm and $h=0.125$ mm, respectively. The reference model consists of explicitly modeled fully resolved 3-D solid fiber and a very fine non-uniform discretization. Within the fiber domain, the average element edge length is approximately $0.33 \mu\text{m}$. The reference model discretization consists of approximately 550,000 elements.

Figure 6 shows the point-wise displacement errors of the proposed XFEM model with respect to the reference simulation for the tensile (Fig. 6a-b) and shear loading (Fig. 6c-d) cases. The point-wise error was computed using the L2-norm for each case and presented as a function of element size in the XFEM discretizations. The six locations at which the point-wise errors are computed are shown in Figs. 5a and refBoundCondition1b.

The errors from the elastic tensile loading example (i.e., no debonding is considered) are shown in Fig. 6a. The errors show monotonic convergence as a function of mesh size. The

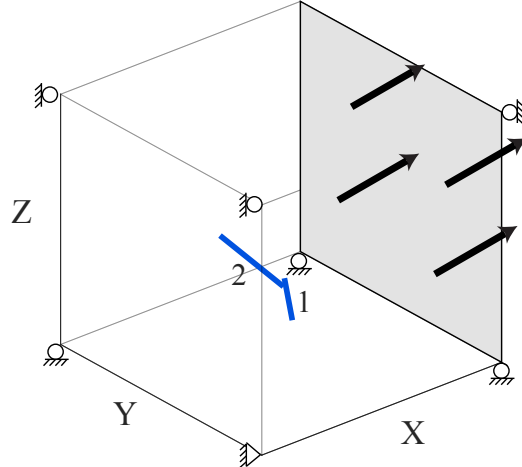


Figure 7: Geometry and boundary conditions of the two fiber inclusion example.

left fiber end (point A1) resulted in the largest error in all cases, but was below 1% for the smallest mesh size. Points C, D, E, and F all had minimal error for all mesh sizes. Figure 6b illustrates the point wise errors corresponding to the case where the progressive debonding between the fiber and the matrix is considered. Similar to the elastic case, the errors showed monotonic mesh convergence, with all errors below 0.25% at the smallest mesh. The largest error occurred at point A1 for all mesh sizes and the errors at the edges of the domain (C, D, E, F) were negligible.

Fig. 6c and 6d display the point wise errors for the elastic and debonding shear loading cases, respectively. The errors from both elastic and debonding cases show a decrease in error with mesh size. The largest errors occurred at the left and right fiber tips (points A1 and B1) for all mesh sizes studied. Similar to the case of tensile loading, the error at the smallest mesh size of $h = 0.125$ mm was approximately below 1.5% for all points considered.

4.2 Two fiber inclusion

In this section, a two fiber inclusion example is studied and compared against the direct finite element method to assess the accuracy of the proposed approach in capturing interfacial debonding and stress. Two fibers are placed neighboring each other in the domain subjected to uniform displacement controlled tensile loading. Figure 7 displays the schematic representation of the two fiber domain. The domain size, the loading and boundary conditions and the constituent interface properties are taken to be the same as in Section 4.1. Both of the fibers in the domain are 1 mm in length and placed at Euler angles of 88° , 55° and 326° , for fiber 1 and at Euler angles of 56° , 41° and 249° , for fiber 2. In this example, the fibers are modeled with progressive debonding along the fiber-matrix interfaces. The orientation of both of the

fibers lie parallel to the direction of the load.

The two-fiber composite domain with the proposed model is discretized using a mesh size of $h=0.125$ mm, resulting in approximately 33,000 elements. The reference simulation, using the direct finite element method, consists of approximately 740,000 elements. Similar to Section 4.1, the fiber domains are completely resolved with a fine grid of solid elements, with the average element edge length approximately $0.33 \mu\text{m}$.

Figure 8 displays the magnitude of the displacement jump along the length of the fibers computed by the proposed model and the reference simulation. For both fibers, the proposed model captures the general shape and magnitude of the displacement jump. The displacement jump for fiber 1 (Fig. 8a), displays approximately the same maximum amplitude over the length of the fiber for both models. In both simulations, the ends of the fiber display a displacement jump. The debonding computed by the proposed model at each of the fiber tips was slightly greater than that of the reference simulation. Figure 8b shows the displacement jump along the fiber length with respect to fiber 2. The shape of the debonding in the proposed model does not match exactly to the reference simulation, but does display similar magnitude and shape. In both fibers, the magnitude of the displacement jump is controlled by the normal displacement jump, since in these examples, the face of the fiber is parallel to the direction of loading. The displacement jump in both fiber 1 and fiber 2 display partial separation across their respective lengths. A three dimensional representation of the progressive debonding in the x, y, and z directions is illustrated in Fig. 9, for (a) a planar view in the X-Y plane, (b) a three dimensional view of the debonding in the domain and (c) a magnified view of the three dimensional debonding. The debonding is amplified ($1e5$ times) to show the magnitude and shape of displacement jumps. The slight discrepancy between the displacement jump profiles computed by the proposed and reference models is attributed to the discretization error introduced by the coarser XFEM mesh especially in capturing the high displacement jump gradients at the fiber tips.

Figure 10(a-b) illustrate the local variation of the normal-stress around fiber 1 as computed by the reference model (Fig. 10a) and the proposed model (Fig. 10b), at the time step when tractions along the interface are near the peak value. The stress contours are from the cross-section parallel to the X-Y plane at $Z=1.75$ mm. In both the reference model and proposed model, the stress field away from the fibers is uniform. Around the fiber, the stress distributions computed by the proposed and reference models are similar. Figures 10c-d compare the stress distributions of the proposed and reference models at a time step, when the interface separations along the fibers are near “maximum” separation (i.e., separation beyond which tractions vanish). Higher stress concentrations are captured by both models at each of the fiber tips. Along the fiber edges, relatively low stresses occur as the tractions unload within the softening regime of the cohesive behavior, past peak tractions.

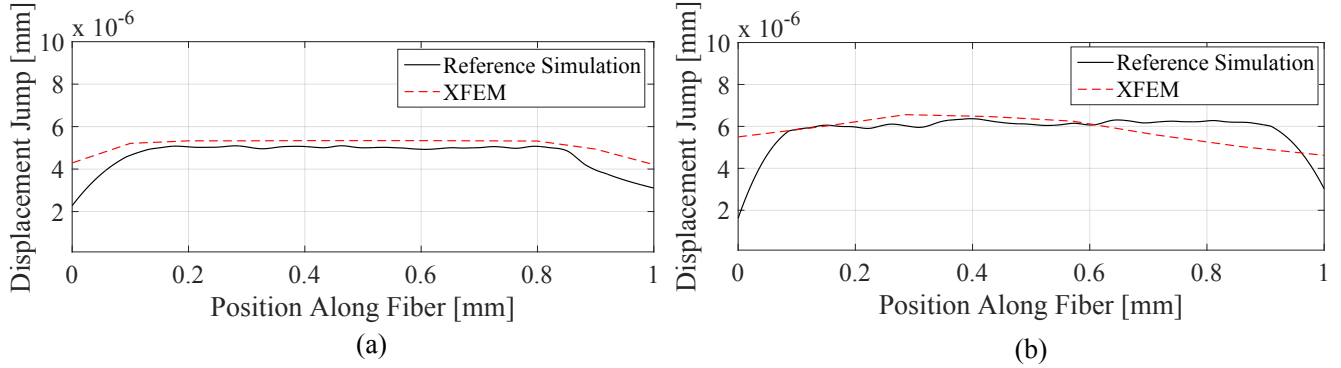


Figure 8: Displacement jump along the fiber length for the two fiber inclusion case: (a) fiber 1; and (b) fiber 2 .

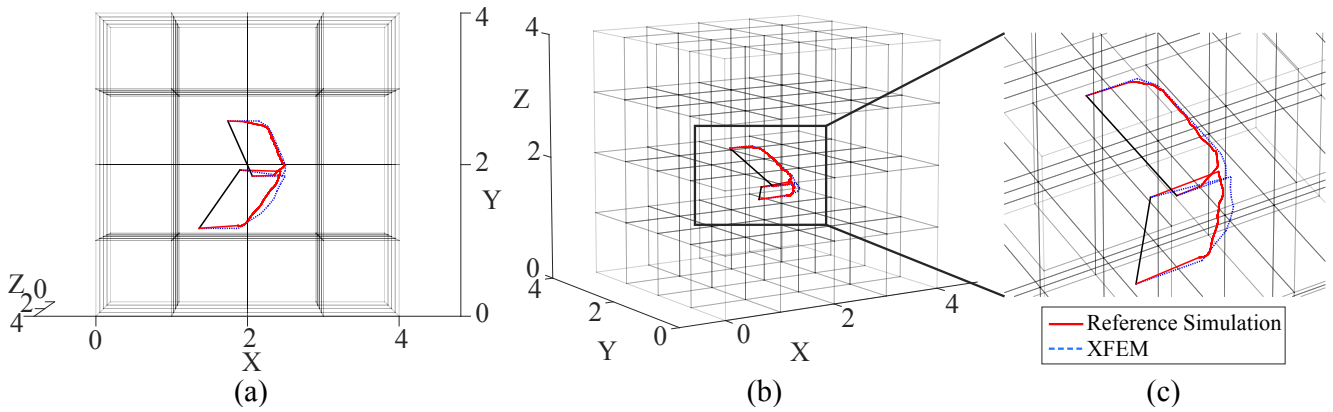


Figure 9: Debonding in a 3-D domain for the two fiber inclusion case: (a) perspective view; (b) 3-D view for debonding (magnitude amplified for visualization); and (c) magnified view. (Solid straight black line represents each fiber, solid red line displays results of the reference model and the blue dotted line is the results of the proposed model.)

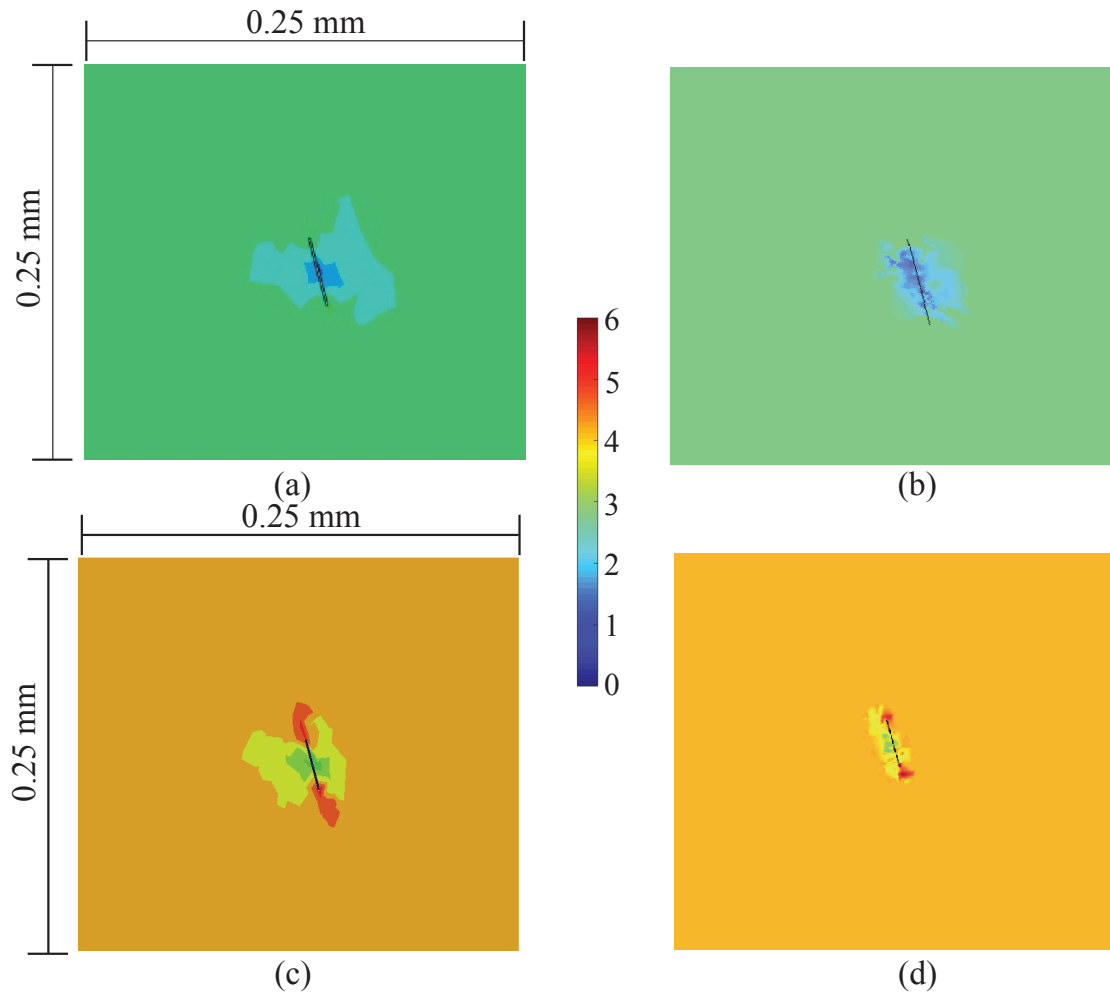


Figure 10: Cross sectional plot of the normal stress in the x direction of fiber 1. Plots taken in the X-Y plane: (a) reference simulation at time step of peak traction; (b) proposed model at time step of peak traction; (c) reference simulation at time step maximum debonding separation; and (d) proposed model at time step of maximum debonding separation.

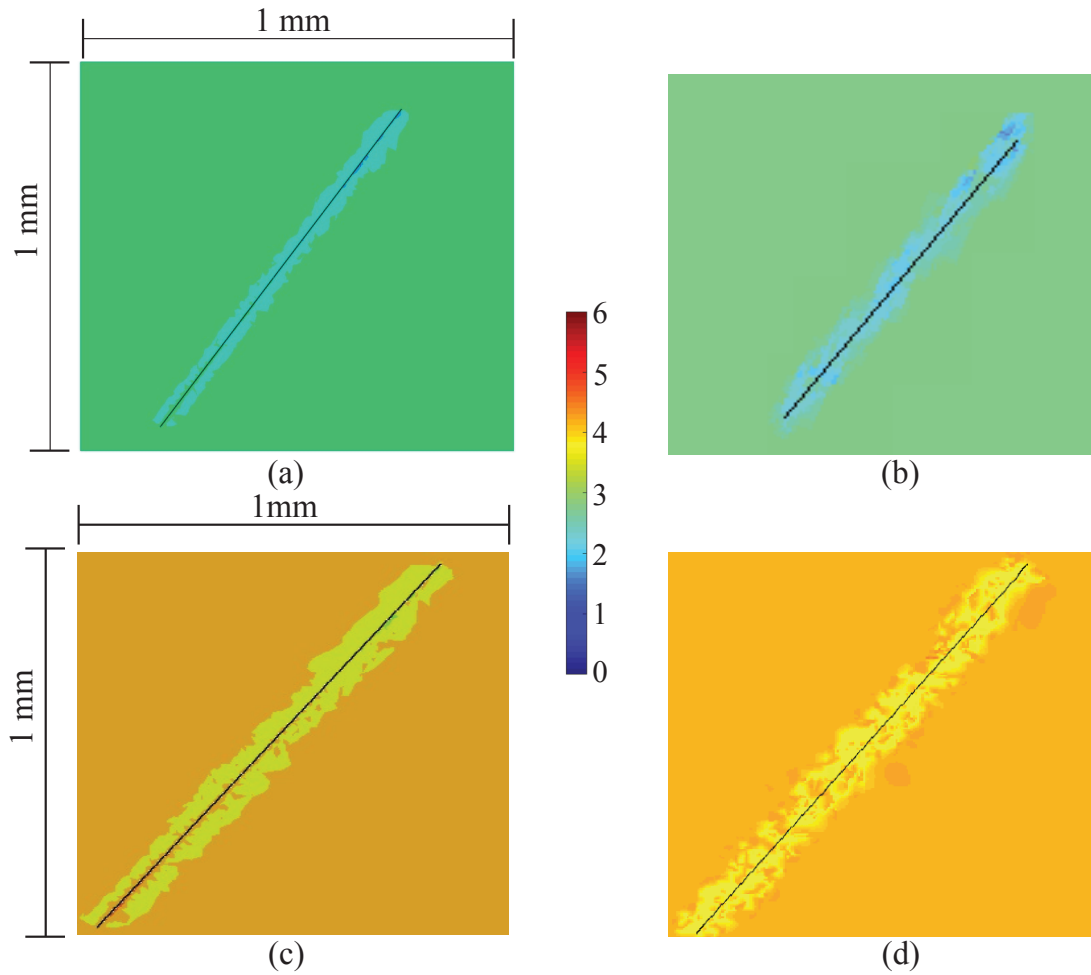


Figure 11: Cross sectional plot of the normal stress in the x direction of fiber 2. Plots taken in the X-Y plane: (a) reference simulation at time step of peak traction; (b) proposed model at time step of peak traction; (c) reference simulation at time step maximum debonding separation; and (d) proposed model at time step of maximum debonding separation.

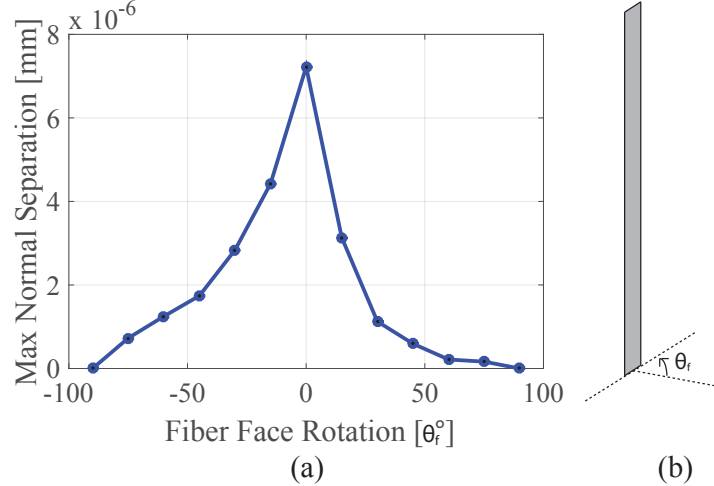


Figure 12: Effect of fiber rotation response: (a) maximum normal separation as a function of the fiber orientation; and (b) fiber orientation with respect to the center of the fiber.

The stress variations around fiber 2 near the peak traction and near maximum separation are displayed in Fig. 11. Figure 11 (a-b) illustrate the local variations in the normal stress around fiber 2 as computed by the reference model (Fig. 11a) and the proposed model (Fig. 11b), at the time step when tractions along the interface are near the peak value. The stress contours are from the cross-section parallel to the X-Y plane at $Z=1.55$ mm. There is a uniform stress field away from the fibers, in both the reference model and proposed model. The computed stress distributions for the proposed model and reference models around the fiber are similar along its length. The stress distribution at a time step, when the interface separations along the fibers are near “maximum” separation are compared in Figs. 11c-d. Along the length of the fiber, slightly lower stresses occur on either side of the fiber as compared with the uniform stress in the domain, similar to fiber 1.

4.3 Effect of fiber orientation

The orientation of the fiber relative to the loading direction significantly affect the response of the composite. In this section, the effect of the orientation of the fiber with respect to the direction of the load is investigated.

The single fiber case discussed in Section 4.1 is modeled with progressive debonding for various fiber orientations. The same material parameters, cohesive law and boundary conditions are used in the example above are employed. The mesh size is set at $h=0.125$ mm for all simulations. The fiber is rotated about its center axis for 13 different angles. The angle is measured at $\theta_f=0^\circ$ for fiber face completely parallel to the direction of the load in the X direction (Fig. 12b). θ_f is rotated every 15° until the fiber face is perpendicular to the direction of the load in both directions.

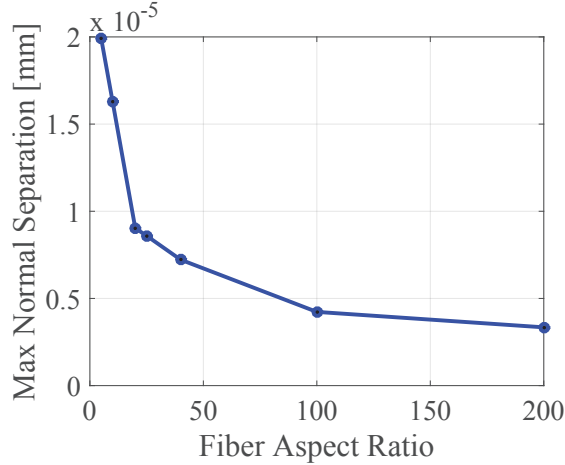


Figure 13: Maximum normal separation as a function of fiber aspect ratio.

The maximum normal separation along the fiber interface is reported in Fig. 12a, for angles ranging from -90° to 90° . Naturally, the maximum normal displacement jump occurs when the fiber face is parallel to the direction of the load. When the fiber is rotated 15° in either direction, there is a steep drop in maximum normal separation at the same load amplitude. The maximum normal separation decreases when the fiber face continues to rotate toward being perpendicular to the load. When the fiber face is completely perpendicular to the load, there is negligible normal separation. It can be seen that the direction of the fiber face influences the response of the fiber-matrix debonding.

4.4 Effect of fiber aspect ratio

We next investigate the effect of the aspect ratio of the fiber (l/w) on the interface debonding properties. A composite with a single fiber, with the orientation of the fiber parallel to the direction of the load, is modeled with various aspect ratios using the proposed XFEM model.

Figure 13 shows the maximum of the normal separations along the fiber length plotted against the fiber aspect ratio at identical load amplitudes. Seven different fiber aspect ratios are modeled ranging from 5 to 200. The largest maximum normal separation occurs with the lowest fiber aspect ratio (5). The maximum normal separation drops as a function of the aspect ratio. There appears to be an exponential decrease of separation with the increase in aspect ratio, with minimal change in separation between the larger aspect ratio fibers. As illustrated, the aspect ratio of the fiber significantly effects the response of the debonding.

4.5 Dense fiber domain

This section investigates a three dimensional dense fiber domain with the proposed XFEM approach for the progressive debonding response. A domain of 4mm x 4mm x 4mm is taken

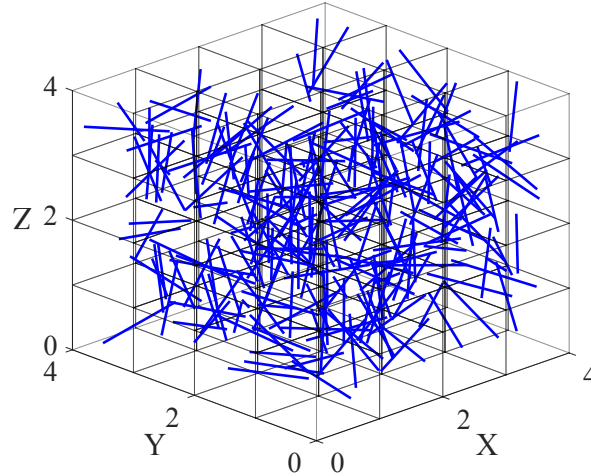


Figure 14: Three dimensional dense fiber domain.

to have 250 randomly oriented fibers in its domain with a mean length of 1 mm (± 0.1 mm), and a fixed width of .02 mm, as displayed in Fig. 14. All 250 fibers are randomly positioned and oriented within the domain. The random dispersion of fibers results in multiple elements having multiple fiber enrichments. Fibers are placed such that they do not touch and do not intersect each other. The mesh size used in this example is $h=0.25$ mm. It should be noted that Fig. 14 does not display the mesh size used in this example, but uses a much larger element size for visualization purposes. The boundary conditions, matrix properties, fiber properties and cohesive law are taken to be the same as in Section 4.1

Figure 15 summarizes the maximum separation at the fiber-matrix interface for each of the fibers. The magnitude range of the maximum separation are categorized in Fig. 15a. There were approximately 100 fibers that resulted in a maximum interface separation of less than $2.5e-6$ mm. 75 fibers had a maximum separation between $2.5e-6$ mm and $5e-6$ mm, 30 fibers had a maximum separation between $5e-6$ mm and $7.5e-6$ mm and 45 fibers resulted in a maximum separation over $7.5e-6$ mm. Fig. 15b displays the severity of debonding. The majority of the fibers in the domain displayed partial separation at their fiber-matrix interface (175 of the 250 fibers). 30 fibers showed no separation and 45 fibers had complete separation at the fiber matrix interface. The varied separations of the fibers occur due to the fiber position and face orientation.

5 Conclusions

The formulation and implementation of an extended finite element method (XFEM) approach for modeling short fiber composites in a three dimensional domain was presented. Short fibers were incorporated into the XFEM framework as elastic two dimensional rectangular planar

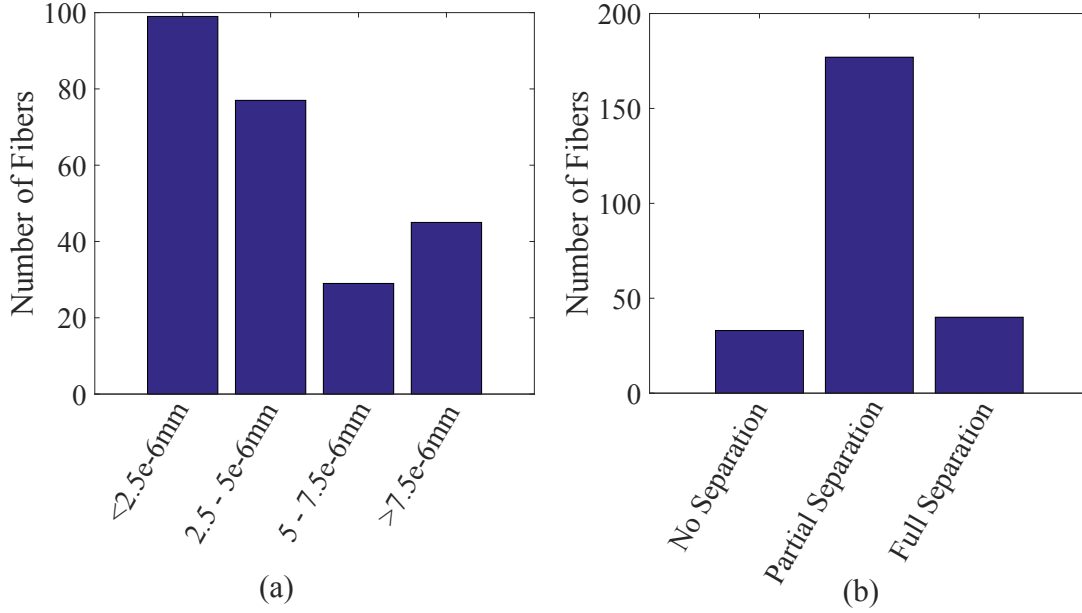


Figure 15: Summary of displacement jumps for the fibers in the dense fiber domain: (a) total number of fibers with their respective maximum separation of each displacement jump; (b) total number of fibers with no separation, partial separation and full separation.

inclusions that were able to deform in the axial direction. A fiber enrichment function to account for the fiber presence and a debonding enrichment function accounting to idealize the progressive debonding on the fiber matrix interfaces were developed. The approach provided a modeling strategy for very high aspect ratio inclusions with fiber matrix debonding capabilities in three dimensions. The performance of the XFEM approach was assessed against the direct finite element method for single and two fiber domains cases and displayed high accuracy. The XFEM model also investigated the response of dense short fiber microstructures.

While the XFEM model in this manuscript works well for the problems analyzed, several challenges remain in more realistic and complicated applications. A key feature that needs to be addressed is the modeling of realistic fiber volume fractions (e.g. 0.5%, 1%) of high aspect ratio fibers in order to compare and reproduce with experiments. Using high aspect ratio fibers to achieve the realistic fiber volume fractions produces a significant amount of fibers in the RVE, which results in numerous fibers in close proximity of each other. This may affect the approximation of the composite and this issue requires further investigation. The interfacial properties can alter various mechanical properties of the composites, including flexural strength and ductility. In this work, the interface properties were considered along the entire length of the fiber-matrix interface, in reality their bond may differ at different locations along the length. Therefore, spatial variability should be considered to accurately access the interfacial response. Furthermore, many of the fibers employed in short fiber reinforced composites have

circular cross sections, which the debonding orientation is dictated by loading direction rather than cross sectional properties. The proposed strategy will be generalized to account for fibers with circular cross sections.

Acknowledgments

The authors gratefully acknowledge the financial support from Vanderbilt University and the Vanderbilt Institute of Software Integrated Systems.

References

- [1] J. Won, B. Hong, T. Choi, S. Lee, and J. Kang. Flexural behaviour of amorphous micro-steel fibre-reinforced cement composites. *Compos. Struct.*, 94:1443–1449, 2012.
- [2] N. Banthia. Uniaxial tensile response of microfibre reinforced cement composites. *Mater. Str.*, 28:507–517, 1995.
- [3] R. Conner, R. Dandliker, and W. Johnson. Mechanical properties of tungsten and steel fiber composites $Zr_{41.25}Ti_{13.75}Cu_{12.5}Ni_{10}Be_{22.5}$ metallic glass matrix composites. *Acta Materialia*, 46:6089–6102, 1998.
- [4] D.D.L. Chung. Cement reinforced with short carbon fibers: a multifunctional material. *Compos. Part B: Engng.*, 31:511–526, 2000.
- [5] F. Reza, J. A. Yamamuro, and G. B. Batson. Electrical resistance change in compact tension specimens of carbon fiber cement composites. *Cement and Concrete Compos.*, 26: 873–881, 2004.
- [6] X. Fu and D. D. L. Chung. Submicron carbon filament cement-matrix composites for electromagnetic interference shielding. *Cement and Concrete Research*, 26:1467–1472, 1996.
- [7] G. P. Tandon and G. J. Weng. Average stress in the matrix and effective moduli of randomly oriented composites. *Compos. Sci. Technol.*, 27:111–132, 1986.
- [8] J. H. Huang. Some closed-form solutions for effective moduli of composites containing randomly oriented short fibers. *Mater. Sci. Engng. A*, 315:11–20, 2001.
- [9] P. Ponte-Castaneda and J.R. Willis. The effect of spatial distribution on the effective behavior of composite materials and cracked media. *J. Mech. Phys. Solids*, 43:1919–1951, 1995.

- [10] H. J. Bohm, A. Eckschlager, and W. Han. Multi-inclusion unit cell models for metal matrix composites with randomly oriented discontinuous reinforcements. *Comp. Mater. Sci.*, 25:42–53, 2002.
- [11] H. R. Lusti, P.J. Hine, and A.A. Gusev. Direct numerical predictions for the elastic and thermoelastic properties of short fibre composites. *Compos. Sci. Technol.*, 62:1927–1934, 2002.
- [12] A.G. Evans and F.W. Zok. The physics and mechanics of fibre-reinforced brittle matrix composites. *J. of Mat. Sci.*, 29:3857–3896, 1994.
- [13] L. Mishnaevsky Jr. and P. Brndsted. Three-dimensional numerical modelling of damage initiation in unidirectional fiber-reinforced composites with ductile matrix. *Mater. Sci. and Engng. A*, 498:81–86, 2008.
- [14] C. Oskay. Variational multiscale enrichment for modeling coupled mechano-diffusion problems. *Int. J. Numer. Meth. Engng.*, 89:686–705, 2012.
- [15] C. Oskay. Variational multiscale enrichment method with mixed boundary conditions for modeling diffusion and deformation problems. *Comput. Meth. Appl. Mech. Engng.*, 264:178–190, 2013.
- [16] S. Zhang and C. Oskay. Variational multiscale enrichment method with mixed boundary conditions for elasto-viscoplastic problems. *Comput. Mech.*, 55:771–787, 2015.
- [17] N. Pan. The elastic constants of randomly oriented fiber composites: A new approach to prediction. *Sci. and Engng. of Compos. Mater.*, 5:63–72, 1996.
- [18] C. Hsueh. Interfacial debonding and fibre pull-out stresses of fibre-reinforced composites. *Mater. Sci. Engng. A*, 123:1–11, 1990.
- [19] A.E. Elwi and T.M Hrudehy. Finite element model for curved embedded reinforcement. *J. Engng. Mech.*, 115:740–754, 1989.
- [20] G.C. Lykidis and K.V. Spiliopoulos. 3D solid finite element analysis of cyclically loaded RC structures allowing embedded reinforcement slippage. *J. Struct. Engng.*, 134:629–638, 2008.
- [21] N. Moës, J. Dolbow, and T. Belytschko. A finite element method for crack growth without remeshing. *Int. J. Numer. Meth. Engng.*, 46:131–150, 1999.
- [22] T. Belytschko and T. Black. Elastic crack growth in finite elements with minimal remeshing. *Int. J. Numer. Meth. Engng.*, 45:601–620, 1999.

- [23] I. Babuska and J. M. Melenk. The partition of unity method. *Int. J. Numer. Meth. Engng.*, 40:727–758, 1997.
- [24] T. Belytschko, N. Moes, S. Usui, and C. Parimi. Arbitrary discontinuities in finite elements. *Int. J. Numer. Meth. Engng.*, 50:993–1013, 2001.
- [25] N. Sukumar and J-H. Prevost. Modeling quasi-static crack growth with the extended finite element method part 1: Computer implementation. *Int. J. Solids and Struct.*, 40:7513–7537, 2003.
- [26] T. Fries and T. Belytschko. The intrinsic XFEM: a method for arbitrary discontinuities without additional unknowns. *Int. J. Numer. Meth. Engng.*, 68:1358–1385, 2006.
- [27] E. Budyn, G. Zi, N. Moes, and T. Belytschko. A method for multiple crack growth in brittle materials without remeshing. *Int. J. Numer. Meth. Engng.*, 61:1741–1770, 2004.
- [28] C. Daux, N. Moes, J. Doblrow, N. Sukumar, and T. Belytschko. Arbitrary branched and intersecting cracks with the extended finite element method. *Int. J. Numer. Meth. Engng.*, 48:1741–1760, 2000.
- [29] B. Hiriyur, H. Waisman, and G. Deodatis. Uncertainty quantification in homogenization of heterogeneous microstructures modeled by XFEM. *Int. J. Numer. Meth. Engng.*, 88:257–278, 2011.
- [30] G. Zi and T. Belytschko. New crack-tip elements for XFEM and applications to cohesive cracks. *Int. J. Numer. Meth. Engng.*, 57:2221–2240, 2003.
- [31] N. Moës and T. Belytschko. Extended finite element method for cohesive crack growth. *Engng. Fract. Mech.*, 69:813–833, 2002.
- [32] N. Sukumar, N. Moes, B. Moran, and T. Belytschko. Extended finite element method for three-dimensional crack modelling. *Int. J. Numer. Meth. Engng.*, 48:1549–1570, 2000.
- [33] N. Sukumar, D.L. Chopp, and B. Moran. Extended finite element method and fast marching method for three-dimensional fatigue crack propagation. *Engng. Fract. Mech.*, 70:29–48, 2003.
- [34] C.A. Duarte, O.N. Hamzeh, T.J. Liszka, and W.W. Tworzydlo. A generalized finite element method for the simulation of three dimensional dynamic crack propagation. *Comput. Meth. Appl. Mech. Engng.*, 190:2227–2262, 2001.

- [35] N. Moes, A. Gravouil, and T. Belytschko. Non-planar 3D crack growth by the extended finite element and level sets Part I: Mechanical model. *Int. J. Numer. Meth. Engng.*, 53: 2549–2568, 2002.
- [36] C. A. Duarte, I. Babuska., and J. Oden. Generalized finite element methods for three-dimensional structural mechanics problems. *Comp. Struct.*, 77:215–232, 2000.
- [37] N. Moës, M. Cloirec, P. Cartraud, and J.-F. Remacle. A computational approach to handle complex microstructure geometries. *Comput. Meth. Appl. Mech. Engng.*, 192: 3163–3177, 2003.
- [38] S. Soghrati and P. H. Geubelle. A 3D interface-enriched generalized finite element method for weakly discontinuous problems with complex internal geometries. *Comput. Meth. Appl. Mech. Engng.*, 217-220:46–57, 2012.
- [39] J. Oswald, R. Gracie, R. Khare, and T. Belytschko. An extended finite element method for dislocations in complex geometries: thin films and nanotubes. *Comput. Meth. Appl. Mech. Engng.*, 198:1872–7886, 2009.
- [40] J.C. Simo, J. Oliver, and F. Armero. An analysis of strong discontinuities induced by strain-softening in rate-independent inelastic solids. *Comp. Mech.*, 12:277–296, 1993.
- [41] M. Jirasek. Comparative study on finite elements with embedded discontinuities. *Comput. Meth. Appl. Mech. Engng.*, 188:307–330, 2000.
- [42] A. Hansbo and P. Hansbo. A finite element method for the simulation of strong and weak discontinuities in solid mechanics. *Comput. Meth. Appl. Mech. Engng.*, 193:3523–3540, 2004.
- [43] C. Oskay. Two-level multiscale enrichment methodology for modeling of heterogeneous plates. *Int. J. Numer. Meth. Engng.*, 80:1143–1170, 2009.
- [44] F.K.F. Radtke, A. Simone, and L.J. Sluys. A partition of unity finite element method for obtaining elastic properties of continua with embedded thin fibres. *Int. J. Numer. Meth. Engng.*, 84:708–732, 2010.
- [45] F.K.F. Radtke, A. Simone, and L.J. Sluys. A partition of unity finite element method for simulating non-linear debonding and matrix failure in thin fibre composites. *Int. J. Numer. Meth. Engng.*, 86:453–476, 2011.

- [46] M. Pike and C. Oskay. Modeling random short nanofiber- and microfiber-reinforced composites using the extended finite-element method. *J. Nanomech. Micromech.*, 5:1–11, 2015.
- [47] M. Pike and C. Oskay. XFEM modeling of short microfiber reinforced composites with cohesive interfaces. *Finite Elements in Analysis and Design*, 106:16–31, 2015.
- [48] M. Pike, M. Hickman, and C. Oskay. Interactions between multiple enrichments in extended finite element analysis of short fiber reinforced composites. *Int. J. Mult. Comput. Engng.*, 2015.
- [49] P. Pierre, R. Pleau, and M. Pigeon. Mechanical properties of steel microfiber reinforced cement pastes and mortars. *J. Mat. Civil Engng.*, 11:317–324, 1999.
- [50] M. Pigeon, R. Pleau, R. Azzabi, and N. Banthia. Durability of microfiber-reinforced mortars. *Cement and Concrete Research*, 26:601–609, 1996.
- [51] V. Gopalaratnam and S. Shah. Tensile failure of steel fiber reinforced mortar. *J. Engng. Mech.*, 113:635–652, 1987.
- [52] D. Lange, C. Ouyang, and S. Shah. Behavior of cement based matrices reinforced by randomly dispersed microfibers. *Adv. Cement Based Mat.*, 3:20–30, 1996.
- [53] CK. Yi and C. Ostertag. Strengthening and toughening mechanisms in microfiber reinforced cementitious composites. *J. Mat. Sci.*, 36:1513–1522, 2001.
- [54] J. Pan and C. K. Y. Leung. Debonding along the FRP - concrete interface under combined pulling/peeling effects. *Engng. Fract. Mech.*, 74:132–150, 2007.
- [55] P. Laborde, J. Pommier, Y. Renard, and M. Salaun. High-order extended finite element method for cracked domains. *Int. J. Numer. Meth. Engng.*, 64:354–381, 2005.
- [56] E. Bechet, H. Minnebo, N. Moes, and B. Burgardt. Improved implementation and robustness study of the X-FEM for stress analysis around cracks. *Int. J. Numer. Meth. Engng.*, 64:1033–1056, 2005.
- [57] K Park, J. Pereira, C. A. Duarte, and G. Paulino. Integration of singular enrichment functions in the generalized/extended finite element method for three-dimensional problems. *Int. J. Numer. Meth. Engng.*, 78:1220–1257, 2009.
- [58] T. Nicholas, D. Boyajian, S.E. Chen, and A. Zhou. Finite element modeling of mode I failure of the single contoured cantilever CFRP-reinforced concrete beam. *J. of Struct.*, 2013:1–8, 2013.